



**Spreading and engulfment of a viscoelastic film onto a Newtonian droplet**Chunheng Zhao *Sorbonne Université and CNRS, Institut Jean Le Rond d'Alembert UMR 7190, F-75005 Paris, France*Taehun Lee *Department of Mechanical Engineering, City College of New York, New York, New York 10031, USA*Andreas Carlson \**Department of Mathematics, Mechanics Division, University of Oslo, Oslo 0316, Norway*

(Received 31 January 2024; accepted 7 August 2024; published 12 September 2024)

We use the conservative phase-field lattice Boltzmann method to investigate the dynamics when a Newtonian droplet comes in contact with an immiscible viscoelastic liquid film. The dynamics of the three liquid phases are explored through numerical simulations, with a focus on illustrating the contact line dynamics and the viscoelastic effects described by the Oldroyd-B model. The droplet dynamics are contrasted with the case of a Newtonian fluid film. The simulations demonstrate that when the film is viscoelastic, the droplet dynamics become insensitive to the film thickness when the polymer viscosity and relaxation time are large. A viscoelastic ridge forms at the moving contact line, which evolves with a power-law dependence on time. By rescaling the interface profile of the ridge using its height and width, it appears to collapse onto a similar shape. Our findings reveal a strong correlation between the viscoelastic stress and the interface shape near the contact line.

DOI: [10.1103/PhysRevFluids.9.094003](https://doi.org/10.1103/PhysRevFluids.9.094003)**I. INTRODUCTION**

Viscoelastic fluids can emerge from the mix of viscous solvents and elastic polymers. These non-Newtonian fluids are found in industrial applications and biological phenomena, such as in three-dimensional (3D) printing [1], fire safety [2,3], mucus [4–6], tissue [7,8], cell rheology [9], and natural convection [10], to name but a few examples. These polymers provide the fluid with an elastic property, causing it to resist deformations. As the viscoelastic fluids undergo deformation, the elastic polymers within them stretch, thus creating a force. In the context of multiphase fluid flows, viscoelastic fluids introduce effects shown to determine the dynamics in processes such as droplet coalescence [11,12], Plateau-Rayleigh instability [13–16], and droplet wetting phenomena [17–21].

When we place a droplet onto a viscous film of another immiscible liquid, the surface tension between droplet-air  $\sigma_{wa}$ , droplet-film  $\sigma_{wv}$ , and film-air  $\sigma_{va}$  will induce contact line motion. Post-contact between the drop and the film, the interfacial dynamics can be decomposed into three parts [22,23]. First, the droplet deforms during a spreadinglike motion as it extends along the film/wall. Second, the film progressively climbs up the droplet and may entirely cover its interface. Third, the droplet is pushed into the film by capillarity. The spreading factor  $S_v = \sigma_{wa} - \sigma_{wv} - \sigma_{va}$  determines the final interfacial shape [23–25]. Theoretically, when  $S_v > 1$ , one would expect the droplet to be fully engulfed by the liquid film. In the case of Newtonian liquids, these dynamics have

\*Contact author: [acarlson@math.uio.no](mailto:acarlson@math.uio.no)

been described by both experiments and numerical simulations, and the process of engulfment is affected by the height of the liquid film/pool [22,23]. A key dimensionless number to describe these dynamics is the Ohnesorge number  $\text{Oh} = \eta_n / \sqrt{\rho_n \sigma_{wn} D}$ , representing the ratio between viscosity and inertia-capillarity, where  $\rho_n$  is the density,  $\eta_n$  is the viscosity, and the subscript  $n$  denotes the Newtonian liquid and  $D$  denotes the droplet diameter.

The applications are evident in fields such as 3D printing and inkjet printing, where the ink interacts with solids coated with various materials [26,27]. In these scenarios, the evolution of the contact angle and the dynamics of the spreading and engulfment processes are critical factors that significantly impact the quality of the print [28]. Additionally, the use of prewetted and liquid-infused surfaces has gained popularity due to their reduced friction characteristics [29,30]. Consider a situation in which a Newtonian fluid in the film is substituted with a viscoelastic fluid, which is expected to introduce new behaviors and potential use in applications. The polymers in the viscoelastic fluid generate an elastic stress, which will affect the dynamics. From a mathematical aspect, the difference between Newtonian fluids and viscoelastic fluids enters into the stress tensor in the Navier-Stokes momentum equations [31]. In addition to the Newtonian viscous contribution, there is an additional nonlinear polymeric contribution in the viscoelastic fluid [13]. While the general effects of viscoelasticity are well-documented, a detailed description of the spreading and engulfment dynamics specific to viscoelastic fluids is missing, which we address in this article by deploying numerical simulations of the three-phase liquid flow with viscoelastic effects.

The description of viscoelastic fluid flow is often based on models such as the upper-convected Maxwell model [32], the Oldroyd-B model, and the FENE-P model [33]. All of these are used to describe the viscoelastic effect and its characteristics. Within these models, there are two important physical parameters, i.e., the polymer viscosity  $\eta_p$  and the polymer relaxation time  $\lambda_p$ , characterizing the viscoelastic properties. The polymer viscosity,  $\eta_p$ , introduces a time-dependent strain rate, dissipating parts of energy within the system, whereas the polymer relaxation time,  $\lambda_p$ , is the timescale required for the system to return to its equilibrium state, or, in simpler terms, how long it takes for stress to relax. If we let these two parameters go towards infinity while maintaining a constant ratio, known as the shear modulus  $G$ , these models have been proposed to model viscoelastic solid systems [13]. Many numerical schemes have been used to tackle the complex flow of viscoelastic fluids [33–35]. Initially, these governing equations were solved by a continuous differential equation for the polymeric stress  $\mathbf{\Pi}_p$  [36,37]. Another computational approach focuses instead on the conformation tensor, which is a geometric tensor that offers a mesoscopic description of the material's structural arrangement [38]. Different numerical methods, such as finite volume [39], finite element [40,41], and finite difference methods, have been used to solve these equations. Nevertheless, when the Weissenberg number is large, representing the ratio between the elastic and viscous forces, the challenge shifts to ensuring the accuracy and stability of the numerical scheme. One way to tackle this is rather than solving the conformation tensor directly, instead compute the evolution of the logarithm of the conformation tensor. This computational methodology ensures the positive-definite nature of the conformation tensor and provides a promising avenue to compute viscoelastic flows [42–44].

Experimental investigations of the coalescence of viscoelastic droplets have shown that compared to Newtonian drop coalescence, viscoelastic droplets exhibit the formation of sharper bridges [12,17]. Accurate interface capturing and curvature estimation in numerical studies is then essential to predict such flows. Different ways to do this include the volume of fluid method [45–49], the level set method [50,51], and the phase-field method, also known as the diffused interface method [52–57], i.e., the interface has a finite thickness. More recently, the conservative phase-field method [58,59] was developed to solve the mass loss problem when simulating small droplets [60,61], which largely improves the efficiency of the fourth-order Cahn-Hilliard equation. In our previous work, the three-phase conservative phase-field lattice Boltzmann method was applied to compute the Newtonian droplet dynamics generated as it meets a perfectly spreading fluid film/pool. In this study, we extend our computational approach by solving the Navier-Stokes equations with a velocity-pressure lattice Boltzmann method [62]. Furthermore, the interface is modeled by the

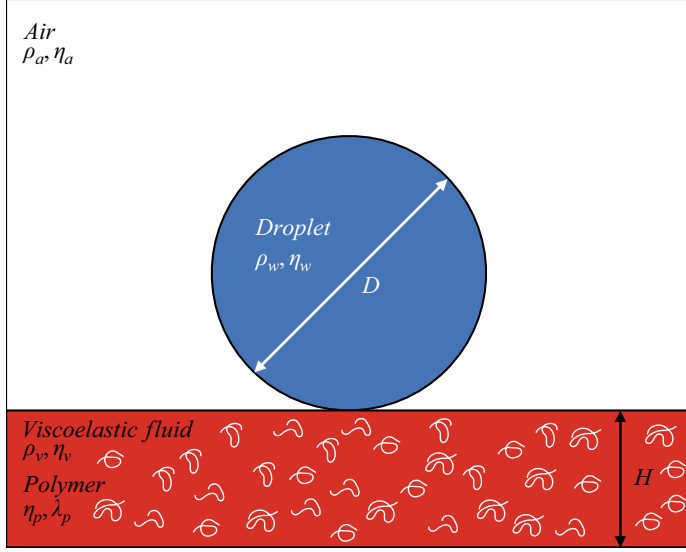


FIG. 1. Schematic of the initial condition of the three-phase fluid flow simulations. The dark blue phase denotes the droplet with density  $\rho_w$ , viscosity  $\eta_w$ , and diameter  $D$ . The red phase represents the viscoelastic fluid solvent with density  $\rho_v$ , viscosity  $\eta_v$ , and height  $H$ , which is filled with polymers of viscosity  $\eta_p$  and relaxation time  $\lambda_p$ . The colorless background represents the surrounding air with density  $\rho_a$  and viscosity  $\eta_a$ .

conservative phase-field lattice Boltzmann method [54,62], and the surface tension is represented by the continuum surface force model [63,64]. The curvature is estimated by the second-order isotropic finite difference method, which greatly improves the numerical performance as introduced in [65]. Below, we will show the 2D simulations of the three-phase flow when a Newtonian droplet comes in contact with an immiscible viscoelastic fluid film.

## II. COMPUTATIONAL METHODOLOGY

### A. Simulation setup

Simulations of the droplet dynamics on a viscoelastic fluid film/pool are conducted on a rectangular domain; see Fig. 1. Initially, we place the droplet with density  $\rho_w$ , viscosity  $\eta_w$ , and diameter  $D$  on the viscoelastic fluid film/pool with density  $\rho_v$ , viscosity  $\eta_v$ , and height  $H$ , filled with a polymer of viscosity  $\eta_p$  and with a relaxation time  $\lambda_p$ . The total viscosity can be expressed as  $\eta_0 = \eta_v + \eta_p$ , and the retardation time is then  $\lambda_2 = \lambda_p \eta_v / \eta_0$ . The initial vertical position of the droplet's center is set as  $c_i = H + 0.5D + 0.01\delta$ , where  $\delta$  is the interface thickness, a nonphysical simulation parameter of the general diffused interface method [52]. The background fluid is composed of air with density  $\rho_a$  and viscosity  $\eta_a$ .

In all simulations, the density and viscosity ratios are fixed as  $\rho_w/\rho_a = \rho_v/\rho_a = 100$ ;  $\eta_v/\eta_a = 1000$ ,  $\eta_w/\eta_a = 100$ . The Ohnesorge number  $\text{Oh} = \eta_v/\sqrt{\rho_v \sigma_{vv} D}$  is used to relate the viscous force to the inertia-capillary force. Normally,  $\text{Oh} \ll 1$  is considered an inertial regime, and  $\text{Oh} \gg 1$  is considered a viscous regime. To characterize the surface tension effect, we introduce the scaled spreading factor of the viscoelastic liquid  $S_v^* = (\sigma_{wa} - \sigma_{wv} - \sigma_{va})/\sigma_{wv}$ . If the spreading factor is positive,  $S_v^* > 0$ , when the droplet is placed on the liquid film, the surface tension force will drive the flow of the liquid in the film, which will gradually cover the droplet. In addition, the height effect is characterized by the initial scaled height of the liquid film, denoted by  $H^* = H/D$ . The parameters mentioned above are based on previous experimental and computational studies, where the surface tension and viscosity ratios are consistent with those observed between air, water/glycerol, and silicone oil. However, the density ratio differs from realistic scenarios. Despite

TABLE I. Physical properties of the liquids used in the ternary flow system.

Parameters	Description	Value
$\rho_v/\rho_a$	density ratio	100
$\rho_v/\rho_w$	density ratio	1
$\eta_v/\eta_a$	viscosity ratio	1000
$\eta_v/\eta_w$	viscosity ratio	10
$\eta^* = \eta_p/\eta_v$	viscosity ratio	1–200
$\text{Cn} = \delta/D$	Cahn number	0.02
$\text{De} = \lambda_p/t_0$	Deborah number	0.025 – 250
$\lambda_2^* = \lambda_2/t_0$	retardation time	$1.75 \times 10^{-4} - 350$
$G^* = \eta^*/De$	shear modulus	0.8 – 8000
$H^* = H/D$	initial film height to drop radius ratio	0.05 – 2
$\text{Oh} = \eta_v/\sqrt{\rho_v\sigma_{wv}D}$	Ohnesorge number	0.05 – 3.7
$\text{Oh}_0 = \eta_0/\sqrt{\rho_v\sigma_{wv}D}$	Ohnesorge number	0.1 – 743.7
$S_v^* = (\sigma_{wa} - \sigma_{wv} - \sigma_{va})/\sigma_{wv}$	Spreading factor	-1.5 – 1.5

this difference, we have validated this setup against experimental results. It is important to note that our current simulations assume small droplet sizes giving a low Bond number ( $\text{Bo} \ll 1$ ), allowing us to disregard the effects of gravity.

We further introduce the polymer into the liquid film/pool, which introduces two important parameters: the viscosity of the polymer  $\eta_p$ , and the relaxation time for the polymer  $\lambda_p$ , which are characterized by two dimensionless numbers: the viscosity ratio  $\eta^* = \eta_p/\eta_v$ , and the Deborah number  $\text{De} = \lambda_p/t_0$ , which is the ratio of the polymer relaxation time and the characteristic flow timescale  $t_0$ . When  $\text{Oh} < 1$ ,  $t_0 = t_\rho = \sqrt{\rho_v D^3/\sigma_{wv}}$ , while  $t_0 = t_\eta = \eta_v D/\sigma_{wv}$  for  $\text{Oh} > 1$ . In the traditional Oldroyd-B model, the retardation time indicates the relationship between the solvent and polymer viscosities, which can be used to characterize the viscoelastic effects. It can be expressed as  $\lambda_2 = \lambda_p \eta_v/\eta_0 = \text{De} t_0/(1 + \eta^*)$ . Additionally, the Oldroyd-B model can be divided to separately consider the polymeric (viscoelastic) and solvent components. In that case, the retardation term is implicitly solved in the solvent part. We will discuss this separation in further detail in Appendix A. We summarize all of the parameter definitions and the values explored in the numerical simulations in Table I.

## B. Governing equations

The mathematical description of the three-phase viscoelastic flow includes the Navier-Stokes equations, the three-phase conservative phase-field equations, and the conformation equation. Those governing equations are listed below:

$$\frac{\partial \bar{p}}{\partial t} + \mathbf{u} \cdot \nabla \bar{p} + c_s^2 \nabla \cdot \mathbf{u} = 0, \quad (1)$$

$$\frac{\partial \mathbf{u}}{\partial t} + \nabla \cdot (\mathbf{u}\mathbf{u}) = -\frac{1}{\rho} \nabla p + \frac{1}{\rho} \nabla \cdot \eta (\nabla \mathbf{u} + (\nabla \mathbf{u})^T) - \frac{3\delta}{2\rho} \sum_{i=1}^3 \sigma_i \nabla \cdot \left( \frac{\nabla \phi_i}{|\nabla \phi_i|} \right) |\nabla \phi_i| \nabla \phi_i + \frac{1}{\rho} \nabla \cdot \mathbf{\Pi}, \quad (2)$$

$$\frac{\partial \phi_i}{\partial t} + \nabla \cdot (\phi_i \mathbf{u}) = \nabla \cdot M \left( \nabla \phi_i - \frac{4}{\delta} \frac{\nabla \phi_i}{|\nabla \phi_i|} \phi_i (1 - \phi_i) + \frac{\phi_i^2}{\sum_{j=1}^3 \phi_j^2} \sum_{j=1}^3 \frac{4}{\delta} \frac{\nabla \phi_j}{|\nabla \phi_j|} \phi_j (1 - \phi_j) \right), \quad (3)$$

$$\mathbf{\Pi} = \frac{\eta_p}{\lambda_p} (\mathbf{A} - \mathbf{I}), \quad (4)$$

$$\frac{\partial \mathbf{A}}{\partial t} + (\mathbf{u} \cdot \nabla) \mathbf{A} = \mathbf{A} \cdot (\nabla \mathbf{u}) + (\nabla \mathbf{u})^T \cdot \mathbf{A} + \frac{1}{\lambda_p} (\mathbf{A} - \mathbf{I}). \quad (5)$$

In the pressure evolution equation, Eq. (1),  $\bar{p} = p/\rho$ , where  $p$  denotes the pressure, and  $\rho$  represents the locally computed density of the three-phase liquid system.  $\mathbf{u}$  represents the velocity vector, and  $c_s$  is the speed of sound.  $\phi_i$  are the liquid phases in the system, represented by the subscript  $i \in [1 - 3]$ . In the velocity evolution equation, Eq. (2),  $\eta(\phi) = \sum_i \phi_i \eta_i$  is the locally computed viscosity of the three-phase liquid system, and  $\delta$  represents the interface thickness [23]. The third term on the right-hand side of Eq. (3) is known as the continuum surface tension force (CSF) [62,63], and the modified surface tension for component  $i$ ,  $\sigma_i$ , is calculated by the surface tension between different components  $\sigma_i = (\sigma_{ij} + \sigma_{ik} - \sigma_{jk})/2$ . Here, we use the three-phase conservative phase-field equation (3) to evolve the order parameter  $\phi_i$ . In the interface region, we have  $0 < \phi_i < 1$ , while in the bulk region of the fluid component  $i$ , we have  $\phi_i = 1$ . The outside of the fluid component  $i$  is denoted as  $\phi_i = 0$ , respectively.  $M$  represents the mobility, which is a model parameter. The influence of  $M$  and  $\delta$  in the conservative phase-field method can be found in [23,66], and in the current study, we fix  $M\Delta t/(\Delta x)^2 = 0.1$  and  $\delta/\Delta x = 4$ , where  $\Delta x$  and  $\Delta t$  are lattice units of length and time given as  $\Delta x = 1$ ,  $\Delta t = 1$ . To solve Eqs. (1), (2), and (3), we employ the velocity-pressure lattice Boltzmann method [62] and the conservative phase-field lattice Boltzmann method [54,62]. In our previous study, we have shown that the conservative phase-field lattice Boltzmann method is able to recreate the experimental three-phase water-oil-air interfacial flow [23]. Therefore, we do not repeat the methodology of the numerical schemes for the momentum equations and the phase-field equations, which are reported in [23].

The last term of Eq. (3) represents the viscoelastic stress  $\mathbf{\Pi}$  and it can be expressed as Eq. (4). We employ the Oldroyd-B model to solve the viscoelastic stress, which can be expressed as Eq. (5). In Eqs. (4) and (5),  $\mathbf{A}$  is the conformation tensor, and  $\mathbf{I}$  represents the identity tensor. In our computational method, the time derivative is solved by a fourth-order Runge-Kutta scheme [67]. The derivatives of the different components are evaluated by the isotropic finite difference method [65]. The details of the numerical method for the conformation equation are presented in the Appendix.

### III. SIMULATION RESULTS

#### A. Evolution of the droplet's center of mass on a viscoelastic fluid film

##### 1. Effect of the height of the viscoelastic fluid film

We start to systematically vary the dimensionless film height of the precoated solid, denoted as  $H^*$ , within both the inertial and viscous regimes. In these numerical experiments, the Deborah number  $De = 0.35$  (for the inertial regime),  $De = 0.25$  (for the viscous regime), and the viscosity ratio  $\eta^* = 200$  are fixed. Figure 2(a) illustrates the evolution of the center of mass  $C_m^* = C_m/D$  with time for different  $H^*$  values in the inertial regime with an Ohnesorge number  $Oh = 0.05$ . To help contrast the Newtonian behavior, we include two dashed reference curves with markers representing Newtonian flow with  $Oh = 0.05$ , corresponding to  $H^* = 0.1, 2$ . There are some noteworthy points to highlight about the behavior of the viscoelastic system. It appears that the dynamics for small  $De$  are fairly insensitive to the relative height  $H^*$ . It can be seen that the final position of the center of mass is close to  $C_m^* = 0.2$ , similar to the Newtonian flow with  $H^* = 0.05$ . However, the viscoelastic nature of the fluid film acts to dampen the inertia-capillary wave that is visible for the Newtonian flow.

In Fig. 2(b), we present the results of a series of simulations conducted within the viscous regime, with  $Oh = 3.7$ . The drop dynamics are insensitive to the thickness of the film. Instead, a master curve for  $C_m^*$  appears following a very similar behavior for the dynamics of a Newtonian droplet on a Newtonian thin liquid film. The simulations of droplet spreading on films with different initial heights are shown in Fig. 3 for the inertial regime ( $Oh = 0.05$ ) and in Fig. 4 for the viscous regime ( $Oh = 3.7$ ).

##### 2. Effect of the polymer relaxation time $\lambda_p$

The droplet dynamics is found to be insensitive to the prewetted film height when the polymer's viscosity is high. The resulting dynamics are then reminiscent of the Newtonian case for a thin prewetted film and it appears that the viscoelastic film becomes more solidlike.

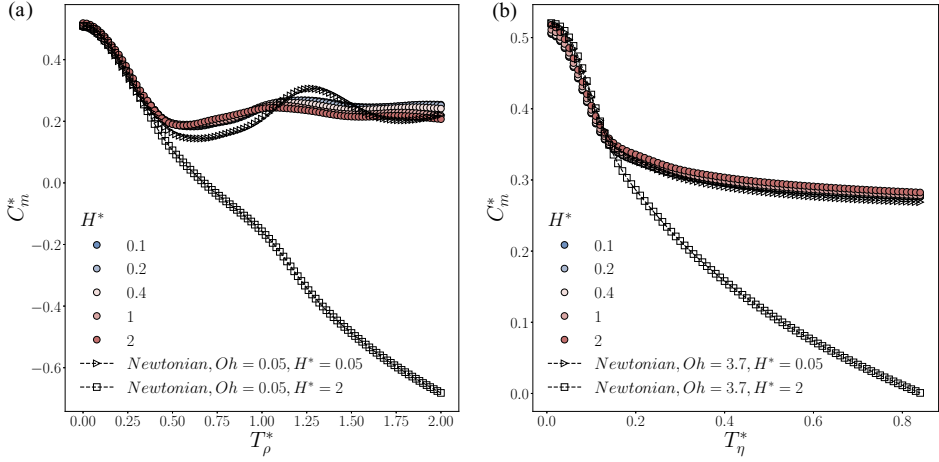


FIG. 2. Evolution of the scaled center of mass ( $C_m^*$ ) position (wall normal) of the droplet on viscoelastic fluid film with varying thickness ( $H^* = [0.05, 2]$ ) during (a)  $T_\rho^* = [0, 2.0]$  for the inertial regime with  $Oh = 0.05$ ,  $De = 0.35$ , and (b)  $T_\eta^* = [0, 0.85]$  for the viscous regime with  $Oh = 3.7$ ,  $De = 0.25$ . The black dashed lines with triangle markers and square markers indicate the results of the Newtonian flow with liquid heights  $H^* = 0.05$  and  $2.0$  for each  $Oh$ , respectively.

Next, we determine how  $De$  affects the viscoelastic engulfment process. We systematically vary  $De$  by adjusting the relaxation time of the polymer, denoted as  $\lambda_p$ . It is worth noting that we fix the viscosity ratio ( $\eta^*$ ) and the liquid film height ( $H^* = 2$ ) throughout these simulations. As demonstrated in Eqs. (4) and (5), the increase in  $\lambda_p$  leads to a reduction in the viscoelastic stress. Additionally, the relaxation term introduced in Eq. (5), denoted as  $(A - I)/\lambda_p$ , diminishes as  $\lambda_p$  increases.

Figure 5(a) illustrates the vertical motion of the droplet's center of mass position for different  $De$  for inertially dominated dynamics  $Oh = 0.05$ . The engulfment process exhibits minimal variation when  $De$  is within the range of  $[0.035, 3.5]$ . However, a substantial deviation from this dynamics is observed for large  $De = 35$ . Intriguingly, when  $De = 350$ , the viscoelastic engulfment process closely resembles that of the Newtonian thin film. The Deborah number controls the polymer relaxation time. As we increase the relaxation time, the polymer takes a long time to recover to its original shape, which makes it behave like a fluid. Therefore, the viscoelastic film with higher Deborah numbers converges to the Newtonian film. The results shown in Fig. 5(b) indicate a similar conclusion for the viscous regime, where  $Oh = 3.7$ . Simulations with different  $De$  are presented in Fig. 6 for the inertial regime ( $Oh = 0.05$ ) and in Fig. 7 for the viscous regime ( $Oh = 3.7$ ).

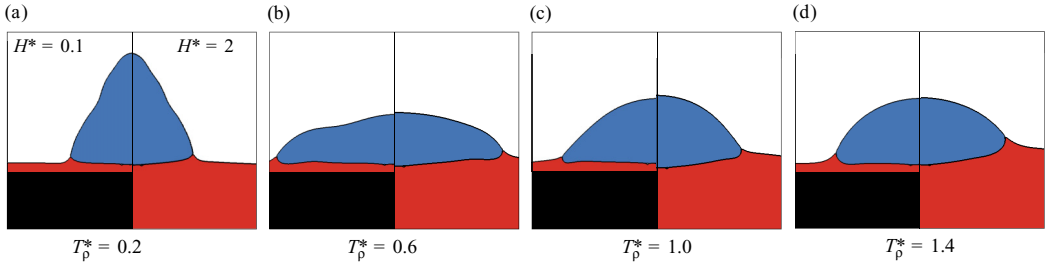


FIG. 3. Simulations of the droplet being spreading on viscoelastic fluid film for  $De = 0.35$ , with different heights  $H^* = 0.1$  (left panel) and  $H^* = 2.0$  (right panel) during  $T_\rho^* = [0.2, 1.4]$  for the inertial regime with  $Oh = 0.05$ .

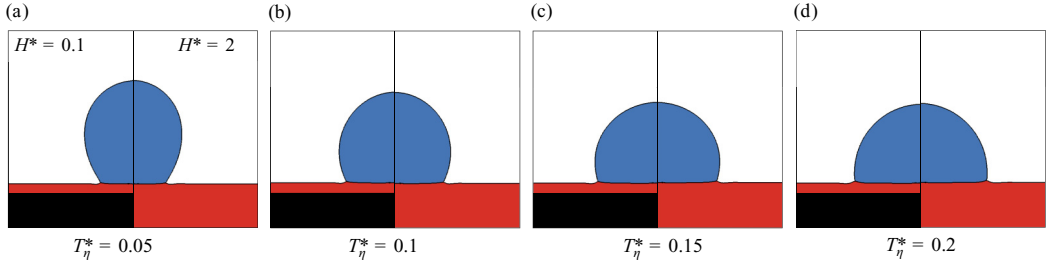


FIG. 4. Simulations of the droplet being spreading on viscoelastic fluid film for  $De = 0.25$ , with different heights  $H^* = 0.1$  (left panel) and  $H^* = 2.0$  (right panel) during  $T_\eta^* = [0.05, 0.2]$  for the viscous regime with  $Oh = 3.7$ .

### 3. Effect of the polymer viscosity $\eta_p$

We conduct additional numerical simulations to determine the influence of the polymer viscosity on the engulfment process. As we systematically increase the polymer viscosity, it becomes increasingly evident that the stress attributed to the polymer induces pronounced changes to the interfacial dynamics.

In Fig. 8(a), we observe the temporal evolution of the center of mass within the inertial regime under varying polymer viscosities. Notably, when the polymer viscosity is relatively low, the engulfment process of the viscoelastic film is fairly similar to the flow of a Newtonian fluid film. However, as we progressively increase the polymer viscosity to sufficiently high levels, the behavior of the liquid film transitions towards that of a solid substrate, exhibiting elastic characteristics. Figure 8(b) demonstrates similar trends within the viscous regime, where due to an increase in polymer viscosity, the evolution of the mass center gradually converges towards that observed in the case of a Newtonian thin film liquid.

We further explore a timescale for the viscous regime where  $Oh > 1$ . Our initial definition of the Ohnesorge number uses the solvent viscosity,  $\eta_v$ . However, we also calculate the Ohnesorge number

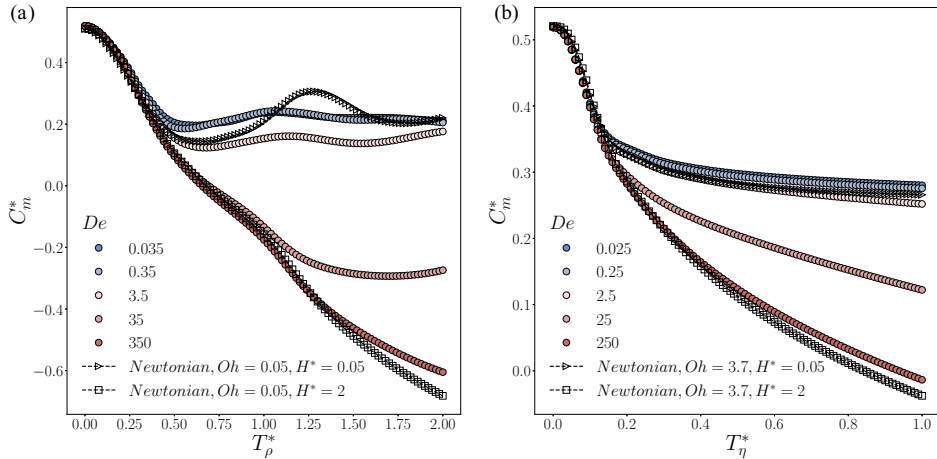


FIG. 5. Evolution of the scaled center of mass ( $C_m^*$ ) position (wall normal) of the droplet on viscoelastic fluid pool with varying relaxation time, during (a)  $T_\rho^* = [0, 2.0]$  for the inertial regime with  $Oh = 0.05$ ,  $De = [0.035, 350]$  and (b)  $T_\eta^* = [0, 1]$  for the viscous regime with  $Oh = 3.7$ ,  $De = [0.025, 250]$ . The black dashed lines with triangle markers and square markers indicate the results of the Newtonian flow with liquid heights  $H^* = 0.05$  and  $2.0$  for each  $Oh$ , respectively.



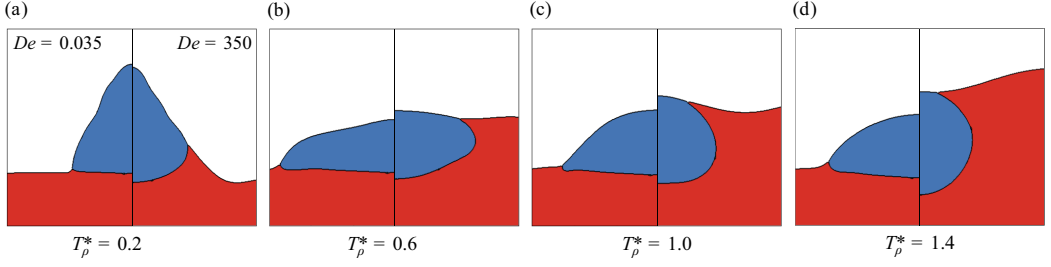


FIG. 6. Simulations of the droplet being spread on a viscoelastic fluid pool with different  $De$ :  $De = 0.035$  (left panel) and  $De = 350$  (right panel) during  $T_p^* = [0.2, 1.4]$  for the inertial regime with  $Oh = 0.05$ .

using the total viscosity, defined as  $Oh_0 = \eta_0 / \sqrt{\rho_v \sigma_{uv} D}$ . Notably, according to this definition, some results previously classified under the inertial regime actually fall within the viscous regime. Inspired by the dynamics of breakup of liquid jets, one may imagine that the observations in Fig. 8 could be reconciled by a timescale accounting for the crossover between inertial and viscous dynamics. In our case, using such a time scale  $(1 + 1.5\sqrt{2}Oh_0)T_p$  [68] does not collapse the data in Fig. 8 onto a master curve, but rather generates a splay in the data. However, we notice that the results shown in Fig. 8(b) is highly dependent on the total viscosity when  $T_\eta^* > 0.15$ . The inset in Fig. 8(b) shows that the data indeed collapse on a single line when shifting for the initial spreading time ( $T_\eta^* = 0.15$ ), where there are minor viscoelastic effects, and rescaling the time with the total viscosity  $T_\eta^*(1 + \eta^*)$ .

#### 4. Summary

We have established that changing the polymer viscosity ( $\eta_p$ ) and the polymer relaxation time ( $\lambda_p$ ) can result in the emergence of an elastic effect limiting the dynamics, while from the governing equation, Eq. (4), we find that the shear modulus  $G = \eta_p / \lambda_p$  determines the magnitude of the viscoelastic forcing. To classify the dynamics, we employ the scaled shear modulus  $G^* = \eta^* / De$  to combine both the effect of the polymer viscosity and the polymer relaxation time. In addition, the retardation time  $\lambda_2$  can characterize the viscoelastic effect as well, and we have a further comparison between using shear modulus and retardation time as our criterion in Appendix A.

To illustrate, we analyze the evolution of the stress components by comparing regions near the contact line for  $G^* = 0.8$  and 80, as depicted in Figs. 9 and 10. The isocontours of the scaled stress tensor components  $\Pi_{11}$  and  $\Pi_{22}$ , which represent the two normal stress components, are shown. The stress values are estimated from the color map on the left, which ranges from  $[-0.16, 0.36]$  for  $G^* = 0.8$  to  $[-6, 5]$  for  $G^* = 80$ . In both scenarios, the conformation tensor  $\mathbf{A}$  solved by Eq. (5) indicates significant deformation near the contact line. The isocontours demonstrate that the viscoelastic stress

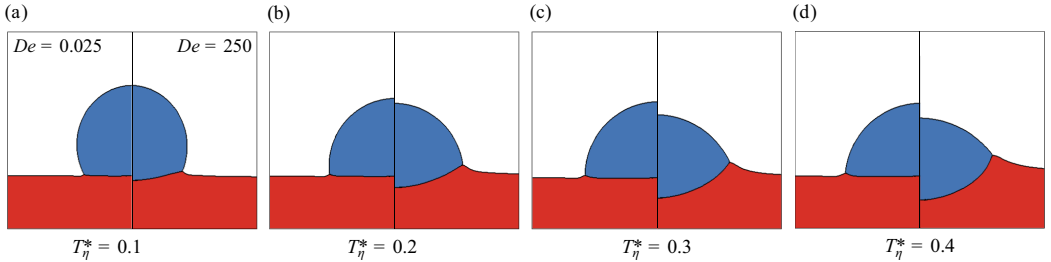


FIG. 7. Simulations of the droplet being spread on viscoelastic fluid pool with different  $De$ :  $De = 0.025$  (left panel) and  $De = 250$  (right panel) during  $T_\eta^* = [0.1, 0.4]$  for the viscous regime with  $Oh = 3.7$ .



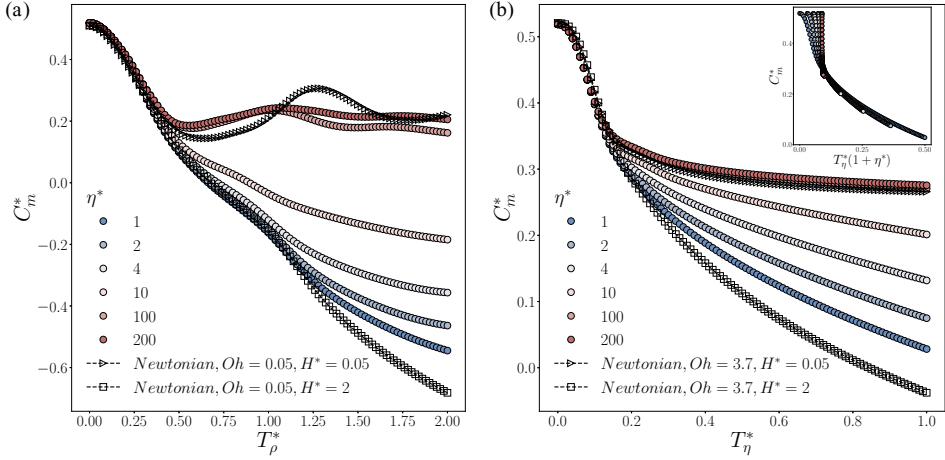


FIG. 8. Evolution of the scaled center of mass ( $C_m^*$ ) position (wall normal) of the droplet on viscoelastic fluid pool with varying polymer viscosity ( $\eta^* = [1, 200]$ ), during (a)  $T_\rho^* = [0, 2.0]$  for the inertial regime with  $Oh = 0.05$ , and (b)  $T_\eta^* = [0, 1]$  for the viscous regime with  $Oh = 3.7$ . The black dashed lines with triangle markers and square markers indicate the results of the Newtonian flow with liquid heights  $H^* = 0.05$  and  $2.0$  for each  $Oh$ , respectively. The inset shows the same data as the main figure, but we have shifted the initial spreading time ( $T_\eta^* = 0.15$ ) and used the total viscosity to scale the time  $T_\eta^*(1 + \eta^*)$ .

distribution within the film is nonuniform. Moreover, a higher shear modulus results in substantial stress, inhibiting further deformation. The viscoelastic effects are confined within the film and exert a pulling force on the contact line in the normal direction relative to the film surface, which also shows why the initial spreading is unaffected by  $G^*$  as shown in Figs. 5 and 8, where  $T_\rho^* < 0.25$  and  $T_\eta^* < 0.2$ . Conversely, the engulfment process, which involves the contact line climbing on the drop, is highly influenced by  $G^*$ .

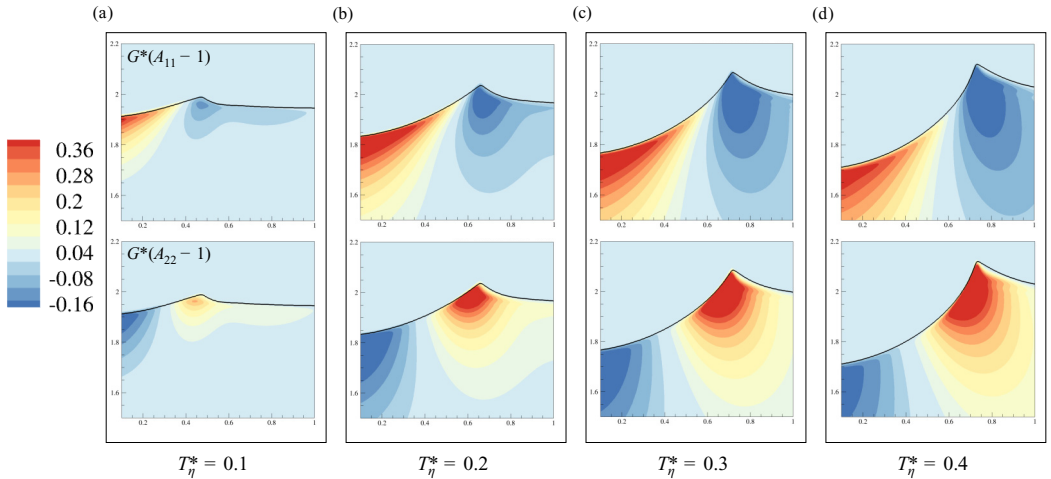


FIG. 9. Scaled stress tensor component  $\Pi_{11}^*$  (top) and  $\Pi_{22}^*$  (bottom) of  $\mathbf{\Pi}^* = G^*(\mathbf{A} - \mathbf{I})$  for  $G^* = 0.8$ ,  $S_v^* = 0.5$ ,  $Oh = 3.7$ ,  $T_\eta^* = [0.1, 0.4]$ . The strain tensor components  $A_{11} - 1$  and  $A_{22} - 1$  are in the range of  $[-0.2, 0.45]$ , and an obvious deformation is observed.

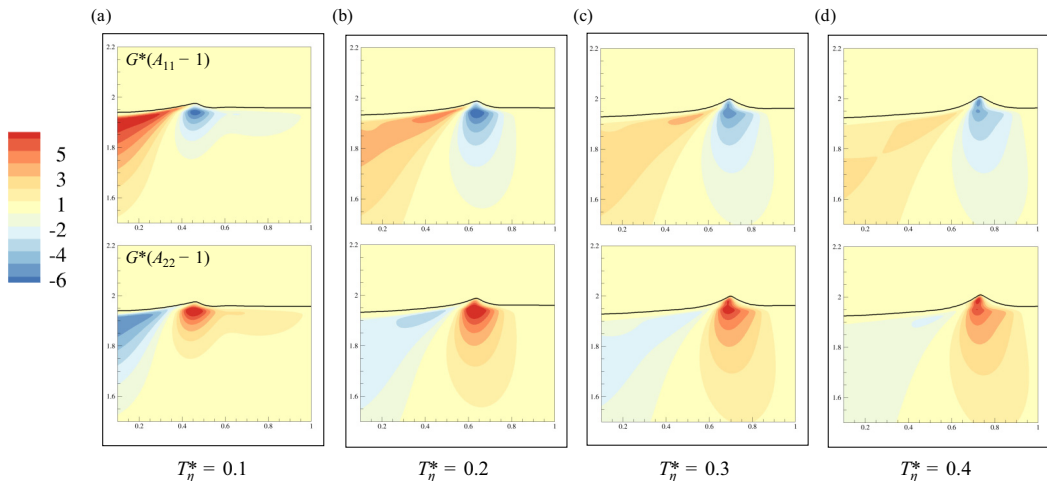


FIG. 10. Scaled stress tensor component  $\Pi_{11}^*$  (top) and  $\Pi_{22}^*$  (bottom) of  $\Pi^* = G^*(\mathbf{A} - \mathbf{I})$  for  $G^* = 80$ ,  $S_v^* = 0.5$ ,  $\text{Oh} = 3.7$ ,  $T_\eta^* = [0.1, 0.4]$ . The strain tensor components  $A_{11} - 1$  and  $A_{22} - 1$  are in the range of  $[-0.075, 0.063]$ , and the deformation is small.

## B. Evolution of the contact angle near the contact line

One particularly interesting aspect to establish is how the viscoelastic effect affects the wetting ridge at the contact line. Previous studies of the deformation of the thin film near the ridge for viscoelastic solids can be found in [69–71]. It is noted that in contrast to works done in [70,71], our simulations are conducted based on the complete Navier-Stokes equations going beyond the thin film approximation. In addition, we consider the fluid flow inside of the viscoelastic film, which highly affects the scaling of the evolution of the meniscus tip with time.

As shown in Fig. 11, the red dotted surface represents the interface ( $\phi_v = 0.5$ ) when  $G^* = 80$ ,  $S_v^* = 1.5$ , and  $\text{Oh} = 3.7$  at  $T_\eta^* = 0.6$ . The contact line, i.e., the point where all phases meet, is marked as the highest vertical point of the interface. The distance from the contact line to the initial interface of the prewetted viscoelastic liquid film (indicated by the black dashed line) is denoted as  $h_c$ , the distance from the contact line to the symmetry axis ( $y$ -axis) is denoted as  $r_c$ , and the width of the wetting ridge (the horizontal distance between the left or the right minimum point of the contact line and the contact surface on another side) is defined as  $w$ . The final shape of the droplet, when placed on a liquid film, is determined by the spreading factor [23]. In this context, the system strives to minimize surface energy. We describe here the dynamics of the formation of the viscoelastic wetting ridge as a function of the spreading factor as well as highlighting the elastic stress distribution.

### 1. Effect of the viscoelastic fluid spreading factor $S_v$

In Fig. 12, we show the evolution of the interface profiles of the viscoelastic wetting ridge around the contact line for different spreading factors: (a)  $S_v^* = -1.5$ , (b)  $S_v^* = 0$ , and (c)  $S_v^* = 1.5$ , where we have fixed the parameters,  $G^* = 80$ ,  $H^* = 2.0$ , and  $\text{Oh} = 3.7$ . The spreading factor dictates the magnitude of the deformation of the viscoelastic film, also affecting the aspect ratio of the wetting ridge.

In Figs. 13(a)–13(c), we present the scaled height, radius, and width of the wetting ridge at the contact line, denoted as  $h^* = (h_c - H)/D$ ,  $r^* = r_c/D$ , and  $w^* = w/D$ , respectively, for the contact line. The spreading factor affects the short-time dynamics when  $T_\eta^* < 0.1$ , where  $h^* \sim (T_\eta^*)^\alpha$ , and  $\alpha$  increases from 0.5 to 0.75 as we change  $S_v^* = [-1.5, 1.5]$ . After  $T_\eta^* > 0.1$ ,  $h^*$  appears to follow the same power-law for different  $S_v^*$ ,  $h^* \sim (T_\eta^*)^{0.6}$ , and  $S_v^*$  mainly affects its prefactor.

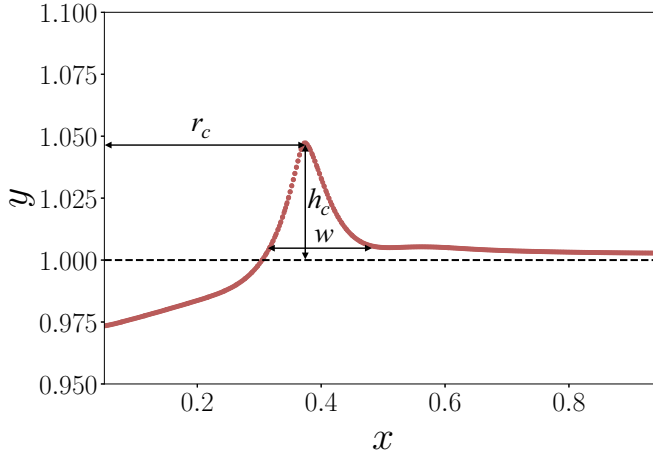


FIG. 11. Interface of the liquid film  $\phi_v = 0.5$  for  $G^* = 80$ ,  $S_v^* = 1.5$ , and  $Oh = 3.7$  when  $T_\eta^* = 0.6$ . The horizontal distance between the contact line to the axis is denoted as  $r_c$ , the distance between the contact line to the initial liquid film interface (indicated by the black dashed line) is denoted as  $h_c$ , and the width of the wetting ridge (the horizontal distance between the left or the right minimum point of the contact line and the contact surface on another side) is defined as  $w$ .

The behavior of the spreading radius  $r^*$  exhibits a similar power-law relationship with time where  $r^* \sim (T_\eta^*)^\beta$ , and  $\beta \approx 0.5$  for the short-time,  $T_\eta^* < 0.1$ . This is consistent with the observations made during spreading on Newtonian fluid films, as noted in previous research [23]. The lack of a viscoelastic effect is likely a consequence of the shear flow, with little extensional effects on the polymers. Nevertheless, after the short-time spreading,  $T_\eta^* > 0.1$ , the spreading factor starts to affect the spreading radius, and it is observed that the power law exponent changes from  $\beta \approx [0.08, 0.25]$ .

We further focus on the width of the wetting ridge after its formation  $T_\eta^* > 0.1$ . As shown in Fig. 13(c), as we modify the spreading factor  $S^* = [-1.5, 1.5]$ , the width of the wetting ridge of different spreading factors follows a similar power law where  $w^* \sim (T_\eta^*)^{0.4}$ . The results indicate the width of the wetting ridge is highly related to the shear modulus but not the spreading factors after short-time evolution.

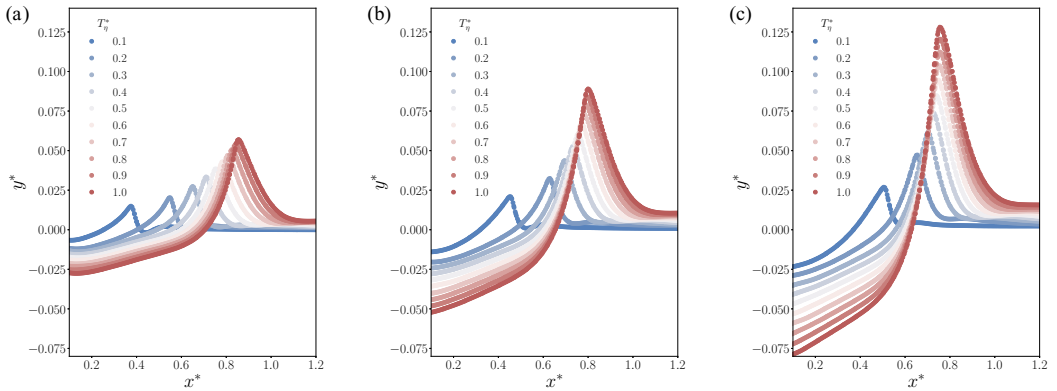


FIG. 12. Evolution of the viscoelastic meniscus for varying the scaled spreading factor  $S_v^*$ , (a)  $S_v^* = -1.5$ , (b)  $S_v^* = 0$ , and (c)  $S_v^* = 1.5$ , during  $T_\eta^* = [0.1, 1]$  in the viscous regime with  $G^* = 80$ ,  $Oh = 3.7$ . The coordinate is scaled by  $x^* = x/D$  and  $y^* = (y - H)/D$ .

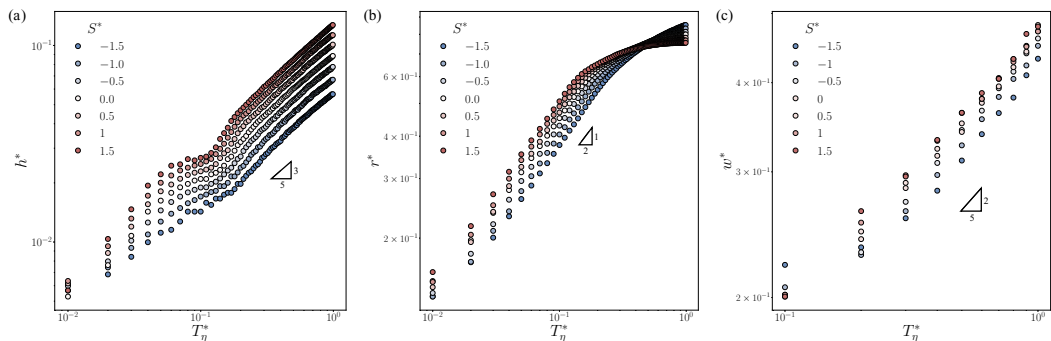


FIG. 13. Evolution of (a) the scaled meniscus height  $h^*$ , (b) the scaled spreading radius  $r^*$  at the meniscus tip during  $T_\eta^* = [0.01, 1]$ , and (c) the scaled width of the wetting ridge  $w^*$  for varying the scaled spreading factor  $S_v^* = [-1.5, 1.5]$  in the viscous regime with  $G^* = 80$ ,  $Oh = 3.7$ .

## 2. Effect of the shear modulus $G^*$

We proceed to explore the influence of polymer viscosity on the wetting ridge dynamics. Throughout these simulations, we fix  $S_v^* = 0.5$  as the spreading factor only shifts the data with a prefactor, while systematically changing  $G^*$ , within the range of  $[0.8, 8000]$  by adjusting the relaxation time,  $\lambda_p$ .

In Figs. 14(a)–14(c), we present the evolution of the interface near the contact line for  $G^* = [0.8, 8000]$ . As seen in the results, the contact line dynamics can be affected by  $G^*$ . As we gradually decrease  $G^*$ , the height of the wetting ridge increases faster, and the liquid film exhibits increased compliance. In the case of  $G^* = 0.8$ , the interface of the liquid film undergoes significant deformation, ultimately resulting in the complete engulfment of the droplet by the liquid film.

In Figs. 15(a) and 15(b), we plot the temporal evolution of  $h^*$  and  $r^*$  in the logarithmic axis. Notably, the vertical ridge position exhibits a behavior affected by  $G^*$ . For a large  $G^* = 8000$ , the evolution of the vertical position can be separated into two distinct regimes: a short-time regime, when  $T_\eta^* < 0.1$ , where it appears that  $h^* \sim (T_\eta^*)^{0.4}$ , followed by  $h^* \sim (T_\eta^*)^{0.6}$ . In contrast, when we decrease  $G^* = 0.8$ , the evolution of  $h^*$  follows a nearly straight line  $h^* \sim T_\eta^*$ . A similar observation is seen in [70], i.e., a linear slope  $h^* \sim T_\eta^*$  can be obtained for different shear modulus, while the

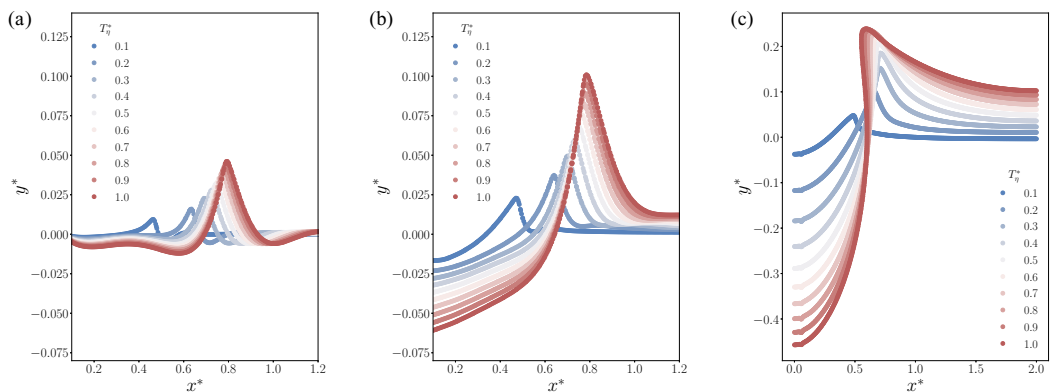


FIG. 14. Evolution of the contact lines between the viscoelastic fluid pool with the air and droplet for varying the scaled shear modulus  $G^*$ , (a)  $G^* = 8000$ , (b)  $G^* = 80$ , and (c)  $G^* = 0.8$ , during  $T_\eta^* = [0.1, 1]$  in the viscous regime with  $S_v^* = 0.5$ ,  $Oh = 3.7$ . The coordinate is scaled by  $x^* = x/D$  and  $y^* = (y - H)/D$ .

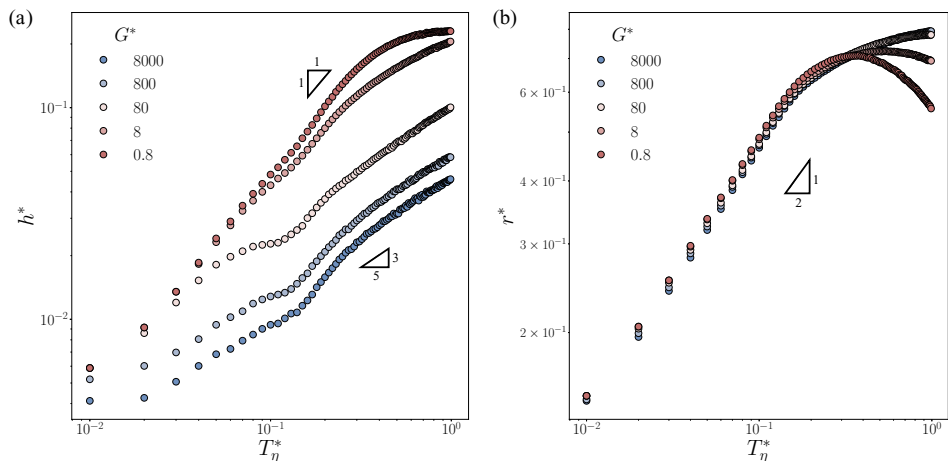


FIG. 15. Evolution of (a) the scaled relevant height  $h^*$ , and (b) the scaled spreading radius  $r^*$  of the contact angle tip for varying the scaled spreading factor  $G^* = [0.8, 8000]$  during  $T_\eta^* = [0.01, 1]$  in the viscous regime with  $S_v^* = 0.5$ ,  $Oh = 3.7$ .

initial spreading stage was not explored in their work. In addition, the coalescence of two droplets will induce different surface effects, which accounts for the difference between their works and our results.

The horizontal position  $r^*$  is contrary to  $h^*$  regardless of  $G^*$ , where  $r^* \sim (T_\eta^*)^{0.5}$ . The effect of  $G^*$  only affects the late-time dynamics associated with the viscoelastic film engulfing the droplet. In the case of small  $G^*$ , the contact line moves across the entire droplet's interface, resulting in a reduction in radius. Conversely, for large  $G^*$ , the spreading process continues but at a much slower rate.

As for the width of the wetting ridge, when we increase the shear modulus  $G^* = [80, 8000]$ , the power law does not change a lot, which follows  $w^* \sim (T_\eta^*)^{0.4}$ . As we decrease  $G^*$ , which lowers the viscoelastic effect, the wetting ridge is not able to be formed. Therefore, it does not follow any power law under such a low shear modulus.

### 3. Relaxation of the contact angle

Figures 16 and 17 illustrate what appears to be a self-similar shape of the wetting ridge for parts of our data set. We have varied here both  $S_v^*$  and  $G^*$ , and we focus on the late-time dynamics, i.e.,  $T_\eta > \lambda_p$ . The wetting ridge of the viscoelastic film is scaled by  $h^*$  and  $w^*$ .

First, when we fix  $G^* = 80$  while changing  $S_v^*$ , we observe that the contact lines associated with different  $S_v^*$  values closely coincide with one another. Specifically, we observe that the radius scaling power  $\beta$  changes from  $\beta \sim [0.08, 0.23]$ , which is consistent with the scaling introduced in the previous section. In addition, the vertical position  $h^*$  follows a similar power law where  $h^* \sim (T_\eta^*)^{0.6}$ . However, a slight counterclockwise rotation is discerned, attributed to the unbalanced surface tension effects.

Second, by fixing  $S_v^* = 0.5$  and changing  $G^* = [0.8, 8000]$ , we observe substantial variations in the interfaces of different simulations. Notably, when  $G^* \gg 1$ , the interface exhibits minimal rotation compared to the short-time profile. The apparent radius of the contact line  $r^* \sim (T_\eta^*)^{0.12}$ , the vertical position of the contact line  $h^* \sim (T_\eta^*)^{0.55}$ , and the width follows  $w^* \sim (T_\eta^*)^{0.4}$ . Conversely, as  $G^*$  decreases, the interface undergoes a more pronounced rotation, and the contact line has a single trend as compared to the cases with higher  $G^*$ .

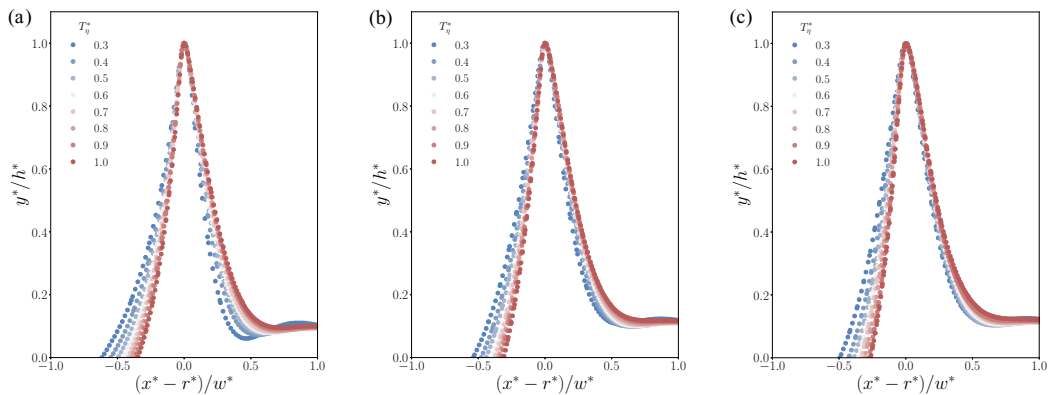


FIG. 16. A seemingly universal shape of the wetting ridge appears when recalling the data with the width and height of the ridge for different scaled spreading factor  $S_v^*$ , (a)  $S_v^* = -1.5$ , (b)  $S_v^* = 0$ , and (c)  $S_v^* = 1.5$ , during  $T_\eta^* = [0.3, 1]$  in the viscous regime with  $G^* = 80$ ,  $Oh = 3.7$ .

#### IV. CONCLUDING REMARKS

In this study, we numerically investigated how viscoelasticity affects the interfacial flow when a Newtonian droplet comes in contact with an immiscible viscoelastic film. As compared to the Newtonian case, a viscoelastic fluid has an influence on the motion of the droplet's center of mass. Numerical experiments establish the influence of the viscoelastic stress, achieved by manipulating polymer viscosity  $\eta_p$  and polymer relaxation time  $\lambda_p$ . When elastic stresses are dominant, we show that the droplet dynamics become insensitive to the thickness of the viscoelastic film in both inertial and viscous flow regimes.

By focusing on the region around the contact line, we observed some intriguing elastic effects in the film. The spreading radius appears completely insensitive to changes in polymer relaxation

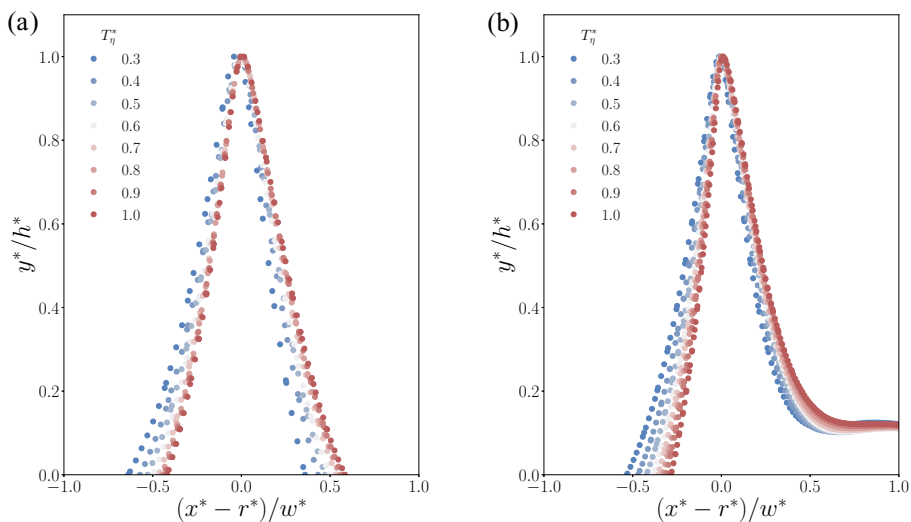


FIG. 17. A seemingly universal shape of the wetting ridge appears when recalling the data with the width and height of the ridge for different  $G^*$ , (a)  $G^* = 8000$  and (b)  $G^* = 80$ , during  $T_\eta^* = [0.3, 1]$  in the viscous regime with  $S_v^* = 0.5$ ,  $Oh = 3.7$ .

time, but the vertical position of the contact line exhibits significant sensitivity to alterations in  $G^*$ . This is a consequence of the generated stresses, which in the radial growth of the droplet induce a shear flow, while the growth in the height of the wetting ridge induces an extensional flow that promotes elastic effects. A noteworthy observation is the formation of sharper bridge profiles induced by polymers, particularly pronounced when the shear modulus  $G^* \gg 1$  is consistent with the coalescence of two viscoelastic droplets [12]. Importantly, our simulations with different spreading factors reveal that while they may influence the final interface morphology, they do not significantly affect the evolution of the wetting ridge. Our findings help to improve our understanding of the interplay between surface tensions, viscoelastic stress, and various influencing parameters in the spreading and engulfment of droplets by viscoelastic liquids. Interesting future avenues of research include theoretically determining the power-law behaviors describing the spreading dynamics and the growth of the wetting ridge, as well as experimentally demonstrating the viscoelastic droplet dynamics observed in the numerical simulations.

### ACKNOWLEDGMENTS

We acknowledge the financial support from the PIRE project ‘‘Multi-scale, Multi-phase Phenomena in Complex Fluids for the Energy Industries,’’ founded by the Research Council of Norway and the U.S. National Science Foundation under Award No. OISE-1743794. This research was supported, in part, under the Research Council of Norway through the program NANO2021 (Project No. 301138) and the National Science Foundation Grants No. CNS-0958379, No. CNS-0855217, No. ACI-1126113, and No. OEC-2215760 (2022), and the City University of New York High Performance Computing Center at the College of Staten Island. The computations were also performed on resources provided by Sigma2 - the National Infrastructure for High-Performance Computing and Data Storage in Norway.

### APPENDIX A

The original Oldroyd-B model can be expressed as

$$\mathbf{T} + \lambda_p \overset{\nabla}{\mathbf{T}} = \eta_0 (\mathbf{D} + \lambda_2 \overset{\nabla}{\mathbf{D}}), \quad (\text{A1})$$

where  $\mathbf{T}$  represents the stress tensor,  $\overset{\nabla}{\mathbf{T}}$  is an upper-convected time derivative of the stress tensor, and  $\mathbf{D} = \nabla \mathbf{u} + (\nabla \mathbf{u})^T$ . In the above equation,  $\lambda_p$  is relaxation time,  $\eta_0 = \eta_v + \eta_p$  is the total viscosity, and the  $\lambda_2 = (\eta_v/\eta_0)\lambda_p$  denotes the retardation time. The upper-convected time derivative can be expressed as:

$$\overset{\nabla}{\mathbf{T}} = \frac{\partial \mathbf{T}}{\partial t} + \mathbf{u} \cdot \nabla \mathbf{T} - [(\nabla \mathbf{u})^T \cdot \mathbf{T} + \nabla \mathbf{u} \cdot \mathbf{T}]. \quad (\text{A2})$$

As we separate the stress tensor into the viscoelastic part and the solvent part  $\mathbf{T} = \boldsymbol{\tau} + \eta_v \mathbf{D}$ , we could then find the viscoelastic stress evolution as

$$\boldsymbol{\tau} + \lambda_1 \overset{\nabla}{\boldsymbol{\tau}} = \eta_p \mathbf{D}. \quad (\text{A3})$$

As we further introduce the conformation tensor  $\mathbf{A}$  where  $\boldsymbol{\tau} = \eta_p (\mathbf{A} - \mathbf{I})/\lambda_1$ , we can derive Eq. (5).

As discussed in Sec. III A, we utilize the scaled shear modulus  $G^*$  to characterize the system. This parameter is intuitively derived from the governing equations. Additionally, parameter  $G^*$  is based on the split equation (A3) which excludes the solvent viscous effect.

The retardation time can be expressed as  $\lambda_2 = t_0/(\text{De}^{-1} + G^*)$ , or dimensionless representation when it is scaled by timescale  $\lambda_2^* = \lambda_2/t_0 = 1/(\text{De}^{-1} + G^*)$ . When  $\eta^* \gg 1$ ,  $G^* \gg \text{De}^{-1}$ , the retardation effect is predominantly governed by the shear modulus  $G^*$ . Conversely, when  $\eta^* \sim 1$ ,  $G^* \sim \text{De}^{-1}$ , the retardation effect cannot be adequately described by the shear modulus alone, which means we also consider the solvent viscous effect. In such scenarios, the solvent viscosity becomes



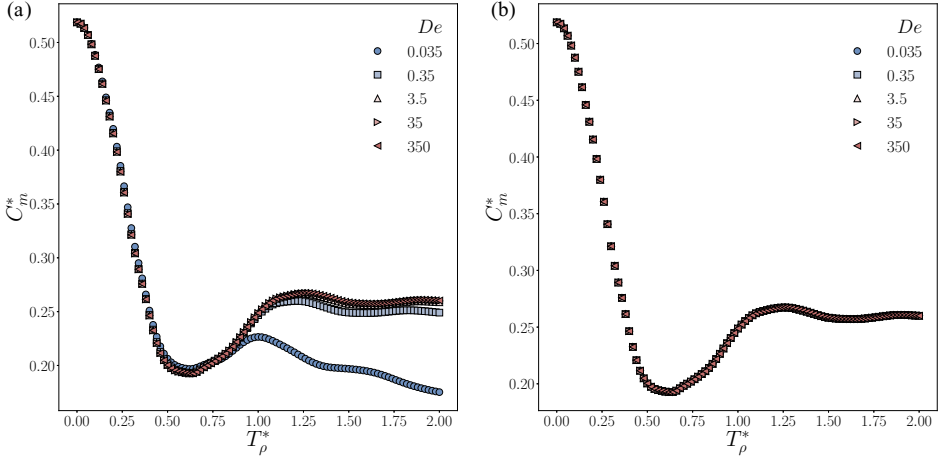


FIG. 18. Mass center evolution of the droplet onto the viscoelastic film with  $Oh = 0.05$ ,  $De = [0.035, 350]$  during  $T_p^* = [0, 2]$ , under (a) the same retardation time  $\lambda_2^*$ , (b) the same shear modulus  $G^*$ .

the dominant factor, causing the fluid to behave like a Newtonian fluid. If  $De$  is decreased while keeping  $\lambda_2^*$  constant,  $G^*$  must also be reduced, which visibly diminishes the viscoelastic effects. As depicted in Fig. 18, differences in the engulfment processes with the same retardation time  $\lambda_2^*$  arise due to the significant variations in  $G^*$ . However, when we keep  $G^*$  constant, we obtain consistent engulfment processes for different  $De$ .

## APPENDIX B

To effectively solve the conformation equation, there exist several methods, i.e., the finite difference method, the lattice Boltzmann method, and the logarithm method [33,44,72–74]. To validate our scheme and study the difference between different numerical methods, we show the comparison of the finite difference method and the logarithm method below.

The discretized conformation equation of Eq. (5) can be shown as

$$\mathbf{A}^{n+1} = \mathbf{A}^n + \Delta t \left[ \mathbf{A} \cdot (\nabla \mathbf{u}^n) + (\nabla \mathbf{u}^n)^T \cdot \mathbf{A} - \frac{1}{\lambda_p} (\mathbf{A} - \mathbf{I}) - (\mathbf{u}^n \cdot \nabla) \mathbf{A} \right]. \quad (\text{B1})$$

To construct a stable system, the Runge-Kutta method is employed, where  $\mathbf{A}^{n+1}$  is approximated by an iterative method. We first evaluate four tensors of slopes  $\mathbf{K}_1, \mathbf{K}_2, \mathbf{K}_3, \mathbf{K}_4$  by

$$\mathbf{K}_1 = -(\mathbf{u}^n \cdot \nabla) \mathbf{A}^n - \frac{1}{\lambda_p} (\mathbf{A}^n - \mathbf{I}) + \mathbf{A}^n \cdot (\nabla \mathbf{u}^n) + (\nabla \mathbf{u}^n)^T \cdot \mathbf{A}^n, \quad (\text{B2})$$

$$\begin{aligned} \mathbf{K}_2 = & -(\mathbf{u}^n \cdot \nabla) (\mathbf{A}^n + 0.5\mathbf{K}_1) - \frac{1}{\lambda_p} ((\mathbf{A}^n + 0.5\mathbf{K}_1) - \mathbf{I}) + (\mathbf{A}^n + 0.5\mathbf{K}_1) \cdot (\nabla \mathbf{u}^n) \\ & + (\nabla \mathbf{u}^n)^T \cdot (\mathbf{A}^n + 0.5\mathbf{K}_1), \end{aligned}$$

$$\begin{aligned} \mathbf{K}_3 = & -(\mathbf{u}^n \cdot \nabla) (\mathbf{A}^n + 0.5\mathbf{K}_2) - \frac{1}{\lambda_p} ((\mathbf{A}^n + 0.5\mathbf{K}_2) - \mathbf{I}) + (\mathbf{A}^n + 0.5\mathbf{K}_2) \cdot (\nabla \mathbf{u}^n) \\ & + (\nabla \mathbf{u}^n)^T \cdot (\mathbf{A}^n + 0.5\mathbf{K}_2), \end{aligned}$$

$$\mathbf{K}_4 = -(\mathbf{u}^n \cdot \nabla) (\mathbf{A}^n + \mathbf{K}_3) - \frac{1}{\lambda_p} ((\mathbf{A}^n + \mathbf{K}_3) - \mathbf{I}) + (\mathbf{A}^n + \mathbf{K}_3) \cdot (\nabla \mathbf{u}^n) + (\nabla \mathbf{u}^n)^T \cdot (\mathbf{A}^n + \mathbf{K}_3).$$

After the evaluation of those slopes, the  $\mathbf{A}^{n+1}$  can be updated as

$$\mathbf{A}^{n+1} = \mathbf{A}^n + \frac{\Delta t}{6} (\mathbf{K}_1 + 2\mathbf{K}_2 + 2\mathbf{K}_3 + \mathbf{K}_4). \quad (\text{B3})$$

Typically, in the lattice Boltzmann method, the time step  $\Delta t = 1$ . In addition to the numerical scheme for conformation tensor  $\mathbf{A}$  we used in the manuscript, we tried the logarithm scheme, which is proven to be valid for the high Weissenberg number problem [73,74]. The essential idea for the logarithm scheme is to alleviate the instability due to the advection-diffusion-reaction equation:

$$\frac{\partial \mathbf{A}}{\partial t} + |\mathbf{u}| \frac{\partial \mathbf{A}}{\partial x} = \frac{1}{\lambda_p} \mathbf{A}. \quad (\text{B4})$$

The stable condition of the discretized equation of Eq. (B4) needs  $\Delta x < \lambda_p |\mathbf{u}|$ , where  $\lambda_p$  has dimension time. When the velocity magnitude  $|\mathbf{u}|$  and the polymer relaxation time  $\lambda_p$  are too small, high resolution is needed to resolve and stabilize the simulation. As we modify the equation to evolve the logarithm of conformation tensor  $\boldsymbol{\psi}$  rather than directly evolving  $\mathbf{A}$ , where  $\boldsymbol{\psi} = \log \mathbf{A}$ , the above Eq. (B4) becomes

$$\frac{\partial \boldsymbol{\psi}}{\partial t} + |\mathbf{u}| \frac{\partial \boldsymbol{\psi}}{\partial x} = \frac{1}{\lambda_p}. \quad (\text{B5})$$

In this case, the discretized equation (B5) is unconditionally stable. We briefly introduce here the numerical method, where a detailed derivation can be found in [44]. Initially, the eigenvalue diagonal matrix  $\boldsymbol{\Lambda}$  and eigenvector tensor  $\mathbf{R}$  of the conformation tensor need to be evaluated, where

$$\mathbf{R}^T \mathbf{A} \mathbf{R} = \boldsymbol{\Lambda}. \quad (\text{B6})$$

The transformation of strain tensor  $\nabla \mathbf{u}$  can then be derived as

$$\nabla \mathbf{u} = \boldsymbol{\Omega} + \mathbf{B} + \mathbf{N} \mathbf{A}^{-1}, \quad (\text{B7})$$

and  $(\nabla \mathbf{u})^T$  is also easily found. Tensor  $\boldsymbol{\Omega}$ ,  $\mathbf{B}$ , and  $\mathbf{N}$  can be computed by the tensor multiplication. Finally, after the transformation, we use the RK4 iterative scheme, which we introduced in the section for the equation:

$$\frac{\partial \boldsymbol{\psi}}{\partial t} + (\mathbf{u} \cdot \nabla) \boldsymbol{\psi} - (\boldsymbol{\Omega} \boldsymbol{\psi} - \boldsymbol{\psi} \boldsymbol{\Omega}) - 2\mathbf{B} = \mathbf{0}. \quad (\text{B8})$$

After we obtain  $\boldsymbol{\psi}^{n+1}$ , we transfer  $\boldsymbol{\psi}$  back to  $\mathbf{A}$ , and we introduce the reaction term  $(\mathbf{A} - \mathbf{I})/\lambda_p$  to finalize the whole process. When the conformation tensor is computed, the same method is employed to introduce the viscoelastic stress to the momentum equation [23].

We first validate the logarithm method and the finite difference method by a benchmark problem of the droplet deformation with a simple shear flow, which is reported in [72,75]. The simulation setup is shown in Fig. 19. We place a droplet with diameter  $D$  into a square with side length  $L = 2D$ . In this case, the density ratio is set to 1. A constant shear velocity  $U = \dot{\gamma} D$  and  $-U$  is applied to the top and bottom boundaries, and the left and right boundary conditions are set as periodic. We characterize this problem by the Deborah number  $\text{De} = \lambda_p \dot{\gamma}$ ,  $\text{Ca} = \dot{\gamma} D \eta_m / \sigma$ , and  $\text{Re} = \rho \dot{\gamma} D^2 / \eta_m$ , where  $\dot{\gamma}$  is the shear rate of the plates, and  $\eta_m$  is the viscosity of the matrix. There are four viscosity property definitions: (1) The matrix viscosity  $\eta_m$ , used to distinguish (2) the droplet viscosity  $\eta_d$ . (3)  $\eta_p$  represents the viscosity of the polymer, and (4)  $\eta_s$  denotes the viscosity of the solvent. To simplify this test, we only test for  $\eta_p = \eta_s$ . When we consider that the matrix is composed of viscoelastic fluid,  $\eta_m = \eta_p + \eta_s = 2\eta_d$ . On the contrary, when the droplet is composed of viscoelastic fluid,  $\eta_d = \eta_p + \eta_s = 2\eta_m$ , respectively.

Both the logarithm method and the finite difference method are applied to simulate four different cases: a Newtonian droplet in a Newtonian matrix (N-N), a Newtonian droplet in a viscoelastic matrix (N-V), a viscoelastic droplet in a Newtonian matrix (V-N), and a viscoelastic droplet in a viscoelastic matrix (V-V), when  $\text{Ca} = 0.48$ ,  $\text{Re} = 1.2$ ,  $\text{De} = 0.4$ . As shown in Figs. 20(a) and 20(b),

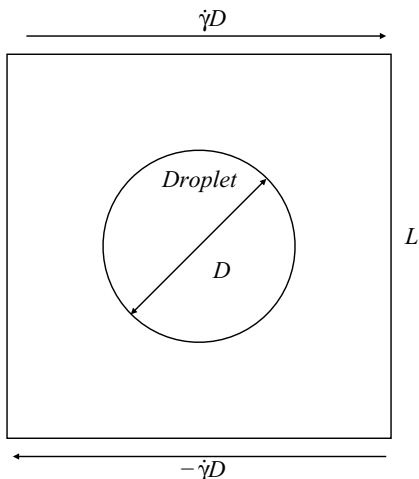


FIG. 19. Initial profile of the single droplet in a simple shear flow.

the temporal evolution of the length parameter  $D^* = (a - b)/(a + b)$  when  $T^* = \dot{\gamma}t = [0, 3]$  for both numerical schemes is highly consistent and in good agreement with [72], where  $a$  and  $b$  are the major and minor axes of the deformed droplet. The deformation of the droplet is relatively greater than that of the viscoelastic matrix when the matrix is made up of Newtonian fluid. Additionally, the deformation of the Newtonian droplet is greater than that of the viscoelastic droplet when the matrix fluid is the same.

Another test is performed to compare two numerical schemes for the three-phase problem. The same setup of the simulations as Sec. III A 2 is employed for both methods to evaluate the effect of  $De$  for the interaction process. Figure 21 shows the comparison of the mass center evolution with  $De = [0.035, 350]$  for different numerical schemes. From the mass center evolution, the difference between the two schemes can be neglected.

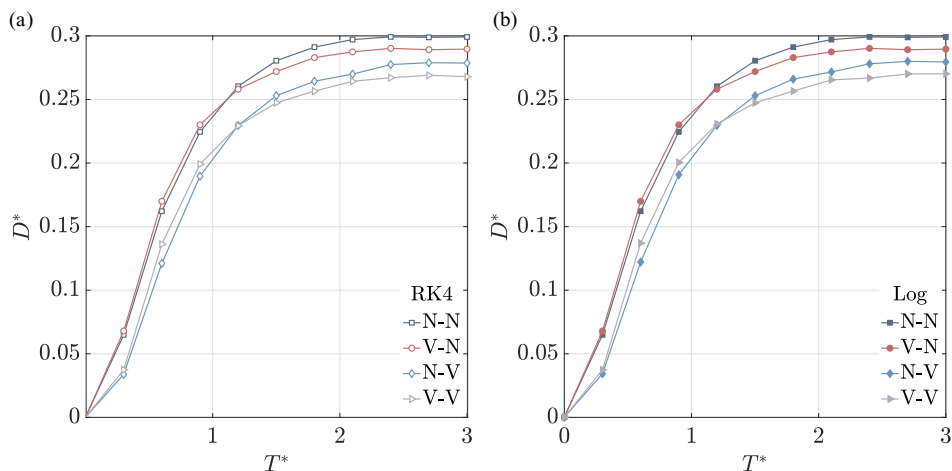


FIG. 20. Evolution of the scaled length parameters in shear flow simulated by (a) finite difference scheme using RK4, and (b) Logarithm scheme.

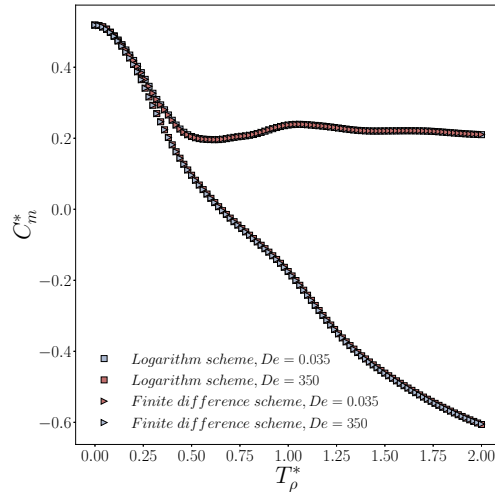


FIG. 21. Comparison between the logarithm scheme and the finite difference scheme.

- [1] C. Duty, C. Ajinjeru, V. Kishore, B. Compton, N. Hmeidat, X. Chen, P. Liu, A. A. Hassen, J. Lindahl, and V. Kunc, What makes a material printable? a viscoelastic model for extrusion-based 3d printing of polymers, *J. Manufacturing Proc.* **35**, 526 (2018).
- [2] M. Jaffe and S. Allam, Safer fuels by integrating polymer theory into design, *Science* **350**, 32 (2015).
- [3] M.-H. Wei, B. Li, R. A. David, S. C. Jones, V. Sarohia, J. A. Schmitgal, and J. A. Kornfield, Megasupramolecules for safer, cleaner fuel by end association of long telechelic polymers, *Science* **350**, 72 (2015).
- [4] M. E. Johansson, H. Sjövall, and G. C. Hansson, The gastrointestinal mucus system in health and disease, *Nat. Rev. Gastroenterol. Hepatology* **10**, 352 (2013).
- [5] S. K. Lai, Y.-Y. Wang, D. Wirtz, and J. Hanes, Micro-and macrorheology of mucus, *Adv. Drug Delivery Rev.* **61**, 86 (2009).
- [6] R. Bansil and B. S. Turner, The biology of mucus: Composition, synthesis and organization, *Adv. Drug Delivery Rev.* **124**, 3 (2018).
- [7] G. Forgacs, R. A. Foty, Y. Shafrir, and M. S. Steinberg, Viscoelastic properties of living embryonic tissues: A quantitative study, *Biophys. J.* **74**, 2227 (1998).
- [8] H. Q. Woodard and D. R. White, The composition of body tissues, *Brit. J. Radiol.* **59**, 1209 (1986).
- [9] P. A. Janmey, U. Euteneuer, P. Traub, and M. Schliwa, Viscoelastic properties of vimentin compared with other filamentous biopolymer networks., *J. Cell Biol.* **113**, 155 (1991).
- [10] I. Pérez-Reyes, R. O. Vargas-Aguilar, S. B. Pérez-Vega, and A. S. Ortiz-Pérez, Applications of viscoelastic fluids involving hydrodynamic stability and heat transfer, *Polymer Rheology*, (IntechOpen, Rijeka, 2018), p. 29.
- [11] S. C. Varma, D. Dasgupta, and A. Kumar, Elasticity can affect droplet coalescence, *Phys. Fluids* **34**, 093112 (2022).
- [12] P. J. Dekker, M. A. Hack, W. Tewes, C. Datt, A. Bouillant, and J. H. Snoeijer, When elasticity affects drop coalescence, *Phys. Rev. Lett.* **128**, 028004 (2022).
- [13] J. Snoeijer, A. Pandey, M. Herrada, and J. Eggers, The relationship between viscoelasticity and elasticity, *Proc. R. Soc. A* **476**, 20200419 (2020).
- [14] N. Wang, S. Li, L. Shi, X. Yuan, and H. Liu, Viscoelastic effects on the deformation and breakup of a droplet on a solid wall in couette flow, *J. Fluid Mech.* **963**, A18 (2023).

- [15] E. Turkoz, J. M. Lopez-Herrera, J. Eggers, C. B. Arnold, and L. Deike, Axisymmetric simulation of viscoelastic filament thinning with the Oldroyd-B model, *J. Fluid Mech.* **851**, R2 (2018).
- [16] F. Li and D. He, Dynamics of a surfactant-laden viscoelastic thread in the presence of surface viscosity, *J. Fluid Mech.* **966**, A35 (2023).
- [17] A. Bouillant, P. J. Dekker, M. A. Hack, and J. H. Snoeijer, Rapid viscoelastic spreading, *Phys. Rev. Fluids* **7**, 123604 (2022).
- [18] C. Henkel, J. H. Snoeijer, and U. Thiele, Gradient-dynamics model for liquid drops on elastic substrates, *Soft Matter* **17**, 10359 (2021).
- [19] D. Greve, S. Hartmann, and U. Thiele, Stick-slip dynamics in the forced wetting of polymer brushes, *Soft Matter* **19**, 4041 (2023).
- [20] S. Yada, K. Bazesfidpar, O. Tammissola, G. Amberg, and S. Bagheri, Rapid wetting of shear-thinning fluids, *Phys. Rev. Fluids* **8**, 043302 (2023).
- [21] C. Zhao, A. Limare, and S. Zaleski, General wetting energy boundary condition in a fully explicit nonideal fluids solver, *Phys. Rev. E* **108**, 055307 (2023).
- [22] C. Cuttle, A. B. Thompson, D. Pihler-Puzović, and A. Juel, The engulfment of aqueous droplets on perfectly wetting oil layers, *J. Fluid Mech.* **915**, A66 (2021).
- [23] C. Zhao, V. R. Kern, A. Carlson, and T. Lee, Engulfment of a drop on solids coated by thin and thick fluid films, *J. Fluid Mech.* **958**, A41 (2023).
- [24] N. Pannacci, H. Bruss, D. Bartolo, I. Etchart, T. Lockhart, Y. Hennequin, H. Willaime, and P. Tabeling, Equilibrium and nonequilibrium states in microfluidic double emulsions, *Phys. Rev. Lett.* **101**, 164502 (2008).
- [25] A. Carlson, P. Kim, G. Amberg, and H. A. Stone, Short and long time drop dynamics on lubricated substrates, *Europhys. Lett.* **104**, 34008 (2013).
- [26] S. Madani and A. Amirfazli, Oil drop shedding from solid substrates by a shearing liquid, *Colloids Surf., A* **441**, 796 (2014).
- [27] S. Hardt and G. McHale, Flow and drop transport along liquid-infused surfaces, *Annu. Rev. Fluid Mech.* **54**, 83 (2022).
- [28] D. Lohse, Fundamental fluid dynamics challenges in inkjet printing, *Annu. Rev. Fluid Mech.* **54**, 349 (2022).
- [29] H. Shams, K. Basit, M. A. Khan, A. Mansoor, and S. Saleem, Scalable wear resistant 3d printed slippery liquid infused porous surfaces (slips), *Addit. Manufacturing* **48**, 102379 (2021).
- [30] M. Villegas, Y. Zhang, N. Abu Jarad, L. Soleymani, and T. F. Didar, Liquid-infused surfaces: A review of theory, design, and applications, *ACS Nano* **13**, 8517 (2019).
- [31] D. D. Joseph, *Fluid Dynamics of Viscoelastic Liquids*, Vol. 84 (Springer Science & Business Media, New York, 2013).
- [32] R. R. Bird, R. C. Armstrong, and O. Hassager, *Dynamics of Polymeric Liquids, Volume 1: Fluid Mechanics* (Wiley-Interscience, Hoboken, New Jersey, 1977).
- [33] M. Alves, P. Oliveira, and F. Pinho, Numerical methods for viscoelastic fluid flows, *Annu. Rev. Fluid Mech.* **53**, 509 (2021).
- [34] S. Aland and P. Auerbach, A ternary phase-field model for wetting of soft elastic structures, *Int. J. Numer. Methods Eng.* **122**, 4114 (2021).
- [35] M. Kloppe and S. Aland, A phase-field model of elastic and viscoelastic surfaces in fluids, *Comput. Methods Appl. Mech. Eng.* **428**, 117090 (2024).
- [36] N. P. Thien and R. I. Tanner, A new constitutive equation derived from network theory, *J. Non-Newtonian Fluid Mech.* **2**, 353 (1977).
- [37] H. Giesekus, A simple constitutive equation for polymer fluids based on the concept of deformation-dependent tensorial mobility, *J. Non-Newtonian Fluid Mech.* **11**, 69 (1982).
- [38] R. B. Bird, R. C. Armstrong, and O. Hassager, *Dynamics of Polymeric Liquids. Vol. 1: Fluid Mechanics*, (Wiley-Interscience, Hoboken, New Jersey, 1987).
- [39] R. G. Owens and T. N. Phillips, *Computational Rheology* (World Scientific, Singapore, 2002).
- [40] A. Davies, S. Lee, and M. Webster, Numerical simulations of viscoelastic flow: The effect of mesh size, *J. Non-Newtonian Fluid Mech.* **16**, 117 (1984).

- [41] Y. Fan, R. I. Tanner, and N. Phan-Thien, Galerkin/least-square finite-element methods for steady viscoelastic flows, *J. Non-Newtonian Fluid Mech.* **84**, 233 (1999).
- [42] R. Fattal and R. Kupferman, Constitutive laws for the matrix-logarithm of the conformation tensor, *J. Non-Newtonian Fluid Mech.* **123**, 281 (2004).
- [43] R. Fattal and R. Kupferman, Time-dependent simulation of viscoelastic flows at high Weissenberg number using the log-conformation representation, *J. Non-Newtonian Fluid Mech.* **126**, 23 (2005).
- [44] J. Hao and T.-W. Pan, Simulation for high Weissenberg number: Viscoelastic flow by a finite element method, *Appl. Math. Lett.* **20**, 988 (2007).
- [45] R. Scardovelli and S. Zaleski, Direct numerical simulation of free-surface and interfacial flow, *Annu. Rev. Fluid Mech.* **31**, 567 (1999).
- [46] S. Popinet, Gerris: A tree-based adaptive solver for the incompressible Euler equations in complex geometries, *J. Comput. Phys.* **190**, 572 (2003).
- [47] C. Zhao, J. Maarek, S. M. Taleghani, and S. Zaleski, A hybrid continuum surface tension force for the three-phase VOF method, *J. Comput. Phys.* **504**, 112872 (2024).
- [48] J. Pan, T. Long, L. Chirco, R. Scardovelli, S. Popinet, and S. Zaleski, An edge-based interface tracking (EBIT) method for multiphase-flow simulation with surface tension, *J. Comput. Phys.* **508**, 113016 (2024).
- [49] T. Long, J. Pan, and S. Zaleski, An edge-based interface tracking (ebit) method for multiphase flows with phase change, *J. Comput. Phys.* **513**, 113159 (2024).
- [50] M. Sussman, P. Smereka, and S. Osher, A level set approach for computing solutions to incompressible two-phase flow, *J. Comput. Phys.* **114**, 146 (1994).
- [51] S. Osher and R. P. Fedkiw, Level set methods: An overview and some recent results, *J. Comput. Phys.* **169**, 463 (2001).
- [52] D. Jacqmin, Calculation of two-phase Navier–Stokes flows using phase-field modeling, *J. Comput. Phys.* **155**, 96 (1999).
- [53] P. Yue, J. J. Feng, C. Liu, and J. Shen, A diffuse-interface method for simulating two-phase flows of complex fluids, *J. Fluid Mech.* **515**, 293 (2004).
- [54] M. Geier, A. Fakhari, and T. Lee, Conservative phase-field lattice Boltzmann model for interface tracking equation, *Phys. Rev. E* **91**, 063309 (2015).
- [55] T. Lee and L. Liu, Lattice Boltzmann simulations of micron-scale drop impact on dry surfaces, *J. Comput. Phys.* **229**, 8045 (2010).
- [56] A. Carlson, M. Do-Quang, and G. Amberg, Dissipation in rapid dynamic wetting, *J. Fluid Mech.* **682**, 213 (2011).
- [57] A. Carlson, M. Do-Quang, and G. Amberg, Modeling of dynamic wetting far from equilibrium, *Phys. Fluids* **21**, 121701 (2009).
- [58] Y. Sun and C. Beckermann, Sharp interface tracking using the phase-field equation, *J. Comput. Phys.* **220**, 626 (2007).
- [59] P.-H. Chiu and Y.-T. Lin, A conservative phase field method for solving incompressible two-phase flows, *J. Comput. Phys.* **230**, 185 (2011).
- [60] P. Yue, C. Zhou, and J. J. Feng, Spontaneous shrinkage of drops and mass conservation in phase-field simulations, *J. Comput. Phys.* **223**, 1 (2007).
- [61] L. Zheng, T. Lee, Z. Guo, and D. Rumschitzki, Shrinkage of bubbles and drops in the lattice Boltzmann equation method for nonideal gases, *Phys. Rev. E* **89**, 033302 (2014).
- [62] C. Zhao and T. Lee, Interaction between a rising bubble and a stationary droplet immersed in a liquid pool using a ternary conservative phase-field lattice Boltzmann method, *Phys. Rev. E* **107**, 025308 (2023).
- [63] J. U. Brackbill, D. B. Kothe, and C. Zemach, A continuum method for modeling surface tension, *J. Comput. Phys.* **100**, 335 (1992).
- [64] J. Kim, A continuous surface tension force formulation for diffuse-interface models, *J. Comput. Phys.* **204**, 784 (2005).
- [65] T. Lee and C.-L. Lin, A stable discretization of the lattice Boltzmann equation for simulation of incompressible two-phase flows at high density ratio, *J. Comput. Phys.* **206**, 16 (2005).

- [66] C. Zhao, Ternary flow simulation based on the conservative phase field Lattice Boltzmann method, Ph.D. thesis, The City College of New York, 2022.
- [67] J. C. Butcher, Implicit Runge-Kutta processes, *Math. Comput.* **18**, 50 (1964).
- [68] J. Eggers and E. Villermaux, Physics of liquid jets, *Rep. Prog. Phys.* **71**, 036601 (2008).
- [69] T. S. Chan, The growth and the decay of a visco-elastocapillary ridge by localized forces, *Soft Matter* **18**, 7280 (2022).
- [70] F. Y. Leong and D.-V. Le, Droplet dynamics on viscoelastic soft substrate: Toward coalescence control, *Phys. Fluids* **32**, 062102 (2020).
- [71] S. Tamim and J. B. Bostwick, Spreading of a thin droplet on a soft substrate, *J. Fluid Mech.* **971**, A32 (2023).
- [72] D. Wang, D. Tan, and N. Phan-Thien, A lattice Boltzmann method for simulating viscoelastic drops, *Phys. Fluids* **31**, 073101 (2019).
- [73] R. Comminal, J. Spangenberg, and J. H. Hattel, Robust simulations of viscoelastic flows at high Weissenberg numbers with the streamfunction/log-conformation formulation, *J. Non-Newton. Fluid Mech.* **223**, 37 (2015).
- [74] J.-M. López-Herrera, S. Popinet, and A.-A. Castrejón-Pita, An adaptive solver for viscoelastic incompressible two-phase problems applied to the study of the splashing of weakly viscoelastic droplets, *J. Non-Newton. Fluid Mech.* **264**, 144 (2019).
- [75] T. Chinyoka, Y. Renardy, M. Renardy, and D. Khismatullin, Two-dimensional study of drop deformation under simple shear for Oldroyd-b liquids, *J. Non-Newton. Fluid Mech.* **130**, 45 (2005).